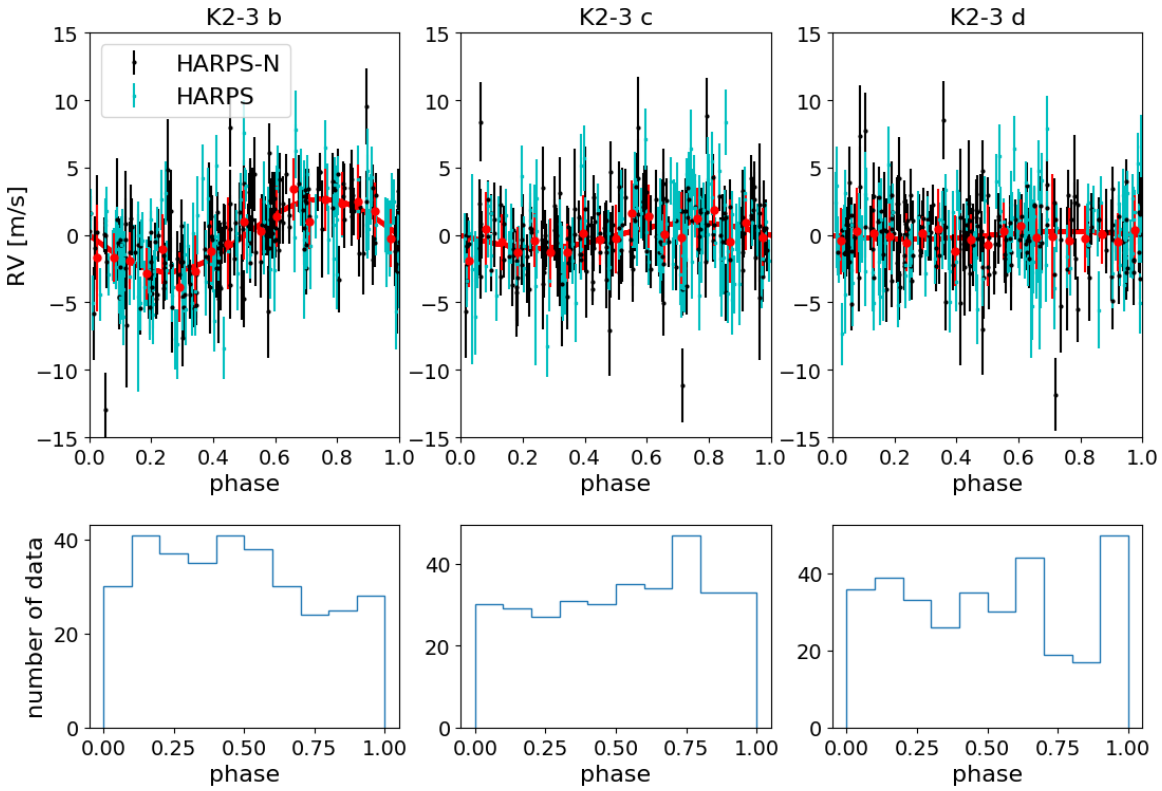

Fig. 8. *First row:* TERRA RV residuals, after removing our best-fit stellar component, phase-folded to the three planetary solutions found for the quasi-periodic GP model (represented by a red curve). *Second row:* histograms of the number of data divided in bins of phase are represented, showing a fairly uniform coverage for each planet.

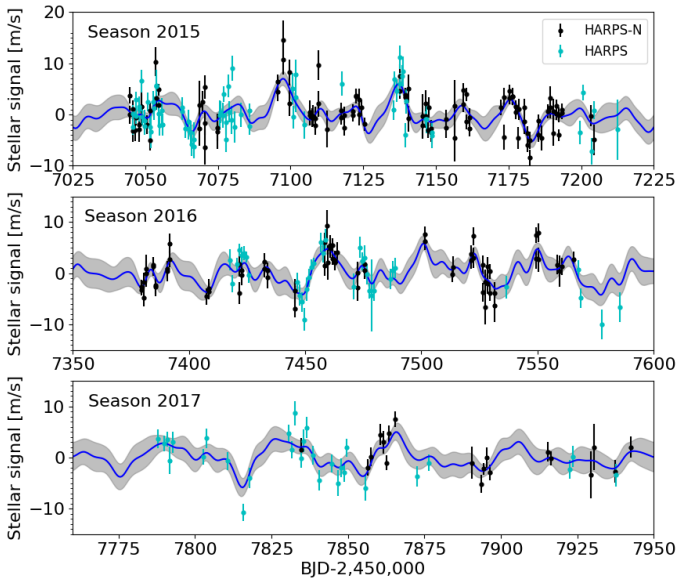

Fig. 9. Stellar signal contribution to the TERRA RV times series, for each observing season, as fitted with our GP quasi-periodic model (Table 3). The blue line indicates the best-fit curve, while the shaded grey area represents the $\pm 1\sigma$ confidence interval.

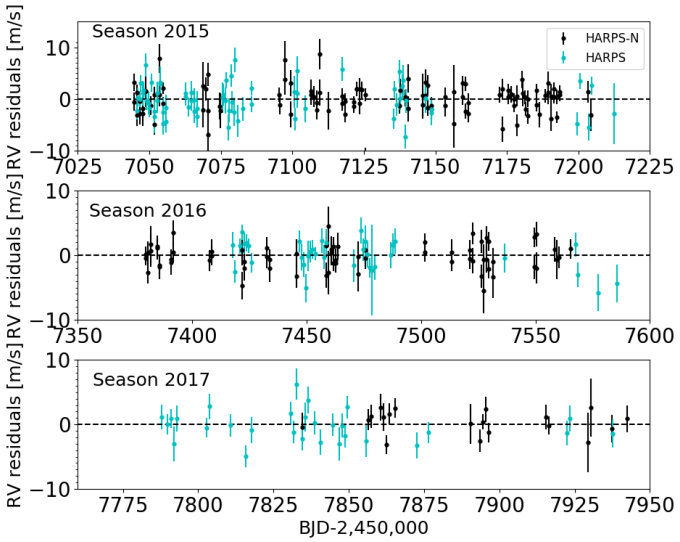

Fig. 10. TERRA RV residuals, after removing the planetary and stellar activity signals, as fitted within a GP quasi-periodic framework (Table 3).

significance of $\sim 7\sigma$, the Doppler signal of K2-3 c is retrieved with a significance lower than 3σ, and K2-3 d is undetected. With the present dataset and the adopted model, we cannot determine a bulk density of K2-3 c accurately enough to put reliable constraints on its possible composition, and we can only place an upper limit on the bulk density of K2-3 d. This impacts our understanding of the formation and evolutionary scenarios, which led to the observed system architecture, and makes inferences about the habitability of K2-3 d especially challenging.

Why is the characterization of this system so challenging, despite the large dataset we have collected with two world-class spectrographs? Can we rule out a rocky composition for K2-3 d? To provide answers to these questions we performed simulations to investigate the impact of the observing sampling, stellar activity, and internal RV uncertainties on our ability to retrieve masses for the K2-3 planets.

5.1. Simulations using real epochs

We ran a first set of simulations based on the real epochs of our observations with the objective to improve the estimate of K2-3 d's mass, for which we could provide only an upper limit, and to assess the robustness of our result for K2-3 c's mass, despite its low significance. First, we adopted our best-fit values of the GP hyperparameters (TERRA dataset) to generate the stellar activity RV signal. We then injected planetary signals (circular orbits) with semi-amplitudes $K_b = 2.7$ m s^{-1}, $K_c = 0.95$ m s^{-1}, and $K_d = 1$ m s^{-1}, and the known periods and times of transit (Table 3) into the simulated activity signal. We refer to the dataset built in this way as the exact solution. While the simulated Doppler semi-amplitudes for K2-3 b and K2-3 c are those we derived from real data, for K2-3 d we assumed a value corresponding approximately to a purely rocky composition, given the measured radius[12].

We then created $N = 156$ mock RV time series[13]. Each dataset was obtained by randomly drawing RV values normally distributed around the exact solution, where $\sigma^2_{RV}(t) + \sigma^2_{jit,instr}$ was used as the variance of the normal distributions at each epoch. We analysed each synthetic dataset following the same procedure as for the real data (Sect. 4.2) and recorded the best-fit values of the free parameters once the MCMC chains reached convergence.

Results from these simulations depend on the actual properties of the stellar activity observed during our campaign. More complex simulations to explore in detail the effects of the stellar activity could also be carried out, where each hyperparameter is randomly drawn within the uncertainties while keeping the others fixed. However, such simulations, which would require a large number of mock datasets (i.e. thousands) and a correspondingly huge amount of computational time, are beyond the scope of this paper. Thus, our simulations do not explore the possibility that the non-detection is due to the proximity of the stellar rotation period θ to the orbital period of K2-3 d, which could be a limiting factor (Vanderburg et al. 2016b). We note that the amplitude h of the stellar activity term is precisely known ($\sim 10\sigma$, Table 3), so we expect that drawing values from the posterior distribution of this hyperparameter would not significantly change the results of our simulations.

Analysis framework. For each ith simulated dataset we derive a posterior distribution for the Doppler semi-amplitudes of planets c and d that we call $K_{p,i}$, where $p = (c, d)$. Each semi-amplitude is characterized by a median value $K^{med}_{p,i}$ and upper and lower uncertainties $\sigma^+_{p,i}$ and $\sigma^-_{p,i}$ (as derived from the 16th and 84th percentiles). We then calculate the median recovered semi-amplitude $K^{med}_{p,N}$ of all the $K^{med}_{p,i}$. We compare the median recovered semi-amplitude $K^{med}_{p,N}$ with the injected value $K_{p,inj}$ to draw conclusions about the results obtained for the real RV dataset.

For K2-3 d, we define the ratio $r_{d,i} = (K_{d,inj}\text{-}K^{med}_{d,i})/\sigma^+_{d,i}$ to measure the discrepancy between the best-fit estimate and the injected value in units of $\sigma^+_{d,i}$. The term $(K_{d,inj}\text{-}K^{med}_{d,i})$ is weighted by $\sigma^+_{d,i}$ to take the skewness of each posterior distribution into account. By averaging $r_{d,i}$ over the number, N, of simulated datasets we get the metric $\bar{r}_d$, that we propose as a way to correct the measured semi-amplitude $K_{d,meas}$ using the equation

$$K_{d,real} = K_{d,meas} + \bar{r}_d \cdot \sigma^+_{d,meas}, \quad (2)$$

where $K_{d,meas}$ and $\sigma^+_{d,meas}$ come from our best-fit solution (Table 3).

As an alternative approach, for each marginal distribution $K_{d,i}$ we calculate the percentile corresponding to the position of $K_{d,inj}$. We use th e median over N of these percentiles to derive an estimate for $K_{d,real}$ from the posterior distribution obtained for the real dataset.

Results for K2-3 c. The distribution of the median values $K^{med}_{c,i}$ is shown in Fig. 11. The median of this distribution is $K^{med}_{c,N} = 0.96^{+0.27}_{-0.22}$ m s^{-1}, where the uncertainties represent the 16th and 84th percentiles. Looking at the values for $\sigma^+_{c,i}$ and $\sigma^-_{c,i}$ over all the marginal posteriors $K_{c,i}$, we note that $\langle(\sigma^+_{c,i}\text{-}\sigma^-_{c,i})\rangle = 0.01$ m s^{-1}, indicating that the distributions are normal-shaped and their average is $\langle\sigma^+_{c,i}\rangle = \langle\sigma^-_{c,i}\rangle = 0.33$ m s^{-1}. These results show that the injected signal $K_{c,inj} = 0.95$ m s^{-1} is well recovered, and indicate that our estimate of K_c from the real dataset is reliable, despite our detection having a significance $<3\sigma$.

Results for K2-3 d. A sample of the N posterior distributions $K_{d,i}$ is shown in Fig. 12. The distribution of $K^{med}_{d,i}$ is shown in Fig. 13. The median of this distribution is $K^{med}_{d,N} = 0.54^{+0.18}_{-0.14}$ m s^{-1}, while we get $\langle\sigma^+_{d,i}\rangle = 0.47$ m s^{-1} and $\langle\sigma^-_{d,i}\rangle = 0.35$ m s^{-1} for the 68.3% confidence interval of each distribution. Therefore, the semi-amplitude K_d is generally underestimated with respect to $K_{d,inj}$. This result is suggestive when compared to what we get for K_c. As shown in Fig. 8, the phase coverage of our data is uniform for planet K2-3 c, and fairly uniform for planet K2-3 d. Then, we would expect two signals with an equal semi-amplitude (here $K_{c,inj} \simeq K_{d,inj}$) to be recovered with similar significance in absence of other hampering factors. For the metric $\bar{r}_d$ we find $\bar{r}_d = 0.99 \pm 0.04$, where the error is calculated as RMS$[r_{d,i}]/\sqrt{N}$. We use this result and our best-fit value for $K_{d,meas} = 0.29^{+0.34}_{-0.18}$ to draw $N = 10\,000$ random values for $\bar{r}_d$ and $K_{d,meas}$, obtaining a distribution of N samples for $K_{d,real}$ from Eq. (2). By taking the median of this distribution and the 68.3% confidence interval we get $K_{d,real} = 0.63^{+0.32}_{-0.18}$ m s^{-1}. This corresponds to $M_{d,real} = 2.7^{+1.2}_{-0.8}$ $M_\oplus$ and $\rho_{d,real} = 3.1^{+2.0}_{-1.2}$ g cm^{-3} for the planet mass and density. Using the second approach mentioned above, we find that $K_{d,real}$ corresponds on average at the 84th percentile of the K_d posterior distribution for the real dataset, that is $K_{d,real} = 0.62$ m s^{-1}, which is a result equal to that obtained with the first method.

Our statistical analysis shows that $K_{d,real}$ is <1 m s^{-1} with 1σ confidence. This in turn suggests that the planets in the K2-3 system may have very similar bulk densities and thus share a similar composition, although this outcome should be taken with caution because of the large uncertainties in the masses and densities for K2-3 c and K2-3 d.

5.2. Role of the observing sampling

We devised new simulations to investigate how the detection significance of the signals induced by the planets K2-3 c and K2-3 d would change by increasing the number of the RV data collected with HARPS-N and HARPS, still assuming $K_d = 1$ m s^{-1}. We simulated an intensive observing strategy conducted during the third season, which has the lowest amount of real data, in a similar way as carried out for the high-cadence campaign devised

[12] $K = 1$ m s^{-1} corresponds to $M_p = 4$ $M_\oplus$.
[13] The number of simulations is as large as possible given the computational expense of a GP analysis on each simulated dataset (up to ~10 h each).

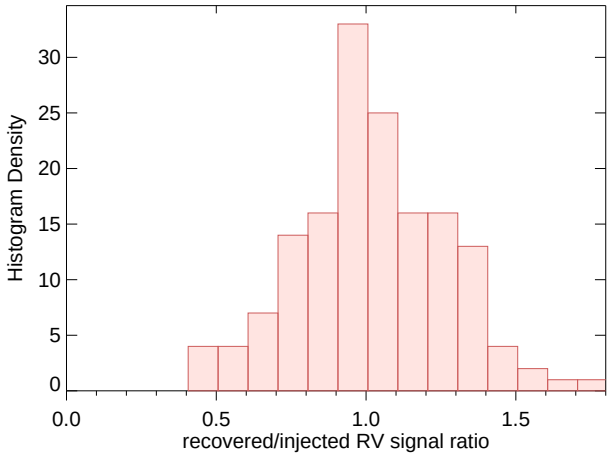

Fig. 11. Distribution of $N = 156$ median values for the Doppler semi-amplitude K_c of planet K2-3 c, normalized to the injected value $K_{c,inj}$, as derived from posterior distributions of the N mock RV datasets. This result refers to the case of real observing epochs.

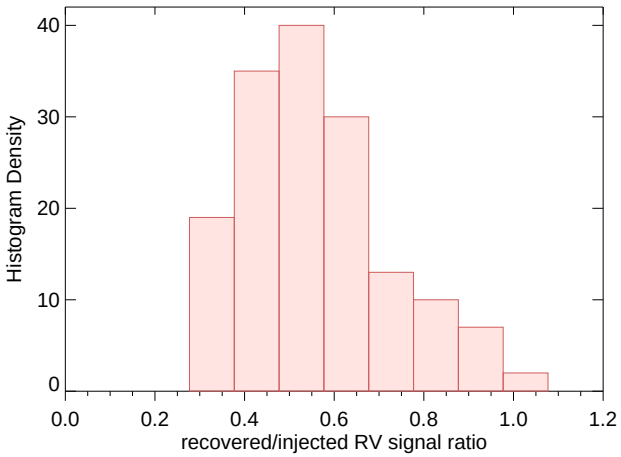

Fig. 13. Distributions of the 50th percentiles for all the posterior distributions of the semi-amplitude K_d obtained from 156 mock datasets, normalized to the injected value $K_{d,inj}$. This result refers to the case of real observing epochs.

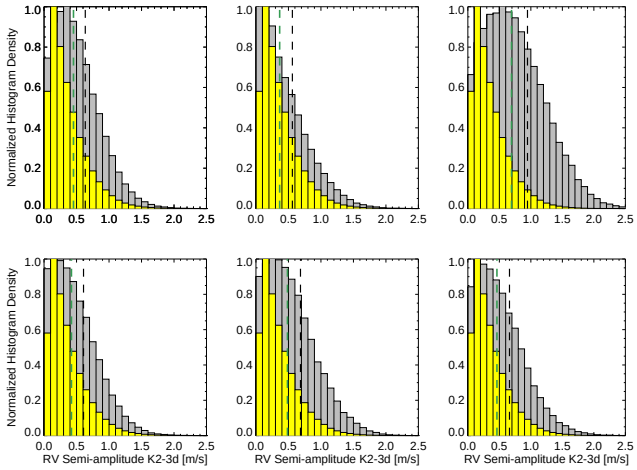

Fig. 12. Sample of posterior distributions (grey histograms) for the Doppler semi-amplitude K_d of planet K2-3 d obtained from the GP regression analysis of the mock RV datasets described in Sect. 5.1. Each plot shows the marginal distribution for a single mock dataset, and this is compared to the posterior distribution obtained for the real TERRA RV dataset, represented by the yellow histogram. The vertical dashed lines indicate the 50th (green) and 68.3th (black) percentiles for the posterior distributions of the mock datasets.

to detect Proxima b with HARPS (Anglada-Escudé et al. 2016). In order to keep our simulation realistic, we did not include mock epochs later than the 2017 observing season because our representation of the RV stellar signal cannot be considered predictive in the far future.

We created the mock datasets as described in Sect. 5.1. We generated all the epochs suitable for observations during the 2017 observing season in addition to the real epochs. We simulated only one measurement per night avoiding superposition with the epochs corresponding to the real observations. Every random epoch was selected by placing constraints on the Moon phase illumination and distance from the target (they have to be <90% and >45°, respectively), and on the altitude of the star above the horizon (airmass <1.7). Using these criteria we got 112 and 100 additional new epochs for HARPS-N and HARPS, respectively. We randomly removed 10% of these epochs at each simulation run to account for bad weather, thus simulating an optimistic scenario for a feasible follow-up[14]. The uncertainties $\sigma_{RV}(t)$ of the mock RV data were randomly drawn from normal distributions with mean and σ equal to the average and RMS values of the HARPS-N and HARPS *post*-upgrade internal errors derived with TERRA. The final mock dataset is obtained by randomly shifting each data point of the exact solution within the error bars by a quantity ΔRV(t) drawn from a normal distribution with mean zero and σ equal to $\sqrt{\sigma^2_{RV}(t) + \sigma^2_{jit}}$. An example mock dataset is show in Fig. 14.

Our final sample is composed of $N = 97$ mock datasets. Also in this case, we analysed each simulated dataset within the same GP quasi-periodic framework applied to the real dataset, except for the σ_{jit} terms that were not included as free parameters, and we analysed the outcomes as described in Sect. 5.1.

Results for K2-3 c. The median and 68.3% confidence interval of the distribution for the $K_{c,i}$ semi-amplitudes are $K_c = 0.96^{+0.27}_{-0.26}$ m s^{-1}. For the upper and lower uncertainties we get $\langle(\sigma^+_{c,i}\text{-}\sigma^-_{c,i})\rangle = 0.006$ m s^{-1} over all the posterior distributions, indicating that they are generally normal-shaped. In addition, $\langle\sigma^+_{c,i}\rangle = \langle\sigma^-_{c,i}\rangle = 0.26$ m s^{-1}. This result not only confirms that the estimate obtained from real data is robust, but also represents an improvement in the significance of the detection that is now increased to 3.7σ.

Results for K2-3 d. The median of the $K_{d,i}$ best-fit values is now $K_d = 0.58^{+0.18}_{-0.15}$ m s^{-1}, while $\langle\sigma^+_{d,i}\rangle = 0.40$ m s^{-1} and $\langle\sigma^-_{d,i}\rangle = -0.34$ m s^{-1}. This result is not very different from that presented in Sect. 5.1, and shows that, despite the 190 additional data to the real dataset, the Doppler signal of K2-3 d is still underestimated and not significantly detected.

6. Discussion and conclusions

This work was focussed on deriving the masses and bulk densities of the three planets transiting the nearby M dwarf K2-3, using 329 RV measurements collected with HARPS and HARPS-N over a period of 2.5 years. We found that stellar activity makes a significant contribution to the RV variations over the entire time period. We have also shown that, for the case

[14] It must be considered that 10% refers to the epochs when K2-3 could actually be observed, not to all the nights of the third season.

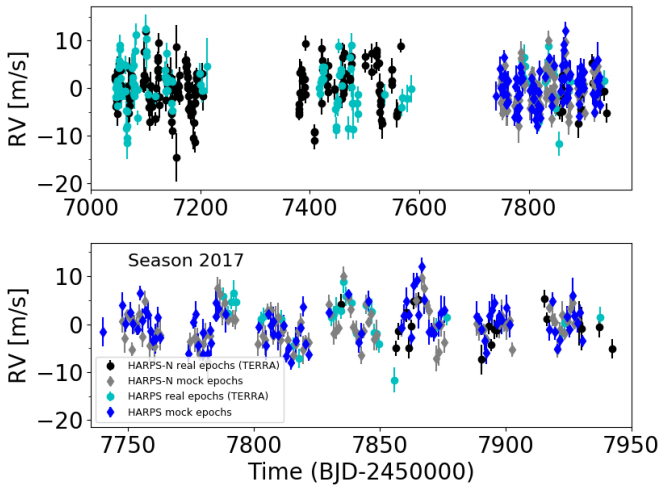

Fig. 14. Example of a simulated RV dataset used to explore the effects on the characterization of the K2-3 planets of additional measurements taken over the 2017 season. The *upper plot* shows the complete mock dataset, while only the third season is shown in the *second plot*, to better appreciate the intensive simulated sampling.

of K2-3, this can be effectively mitigated using a GP regression with a quasi-periodic kernel. The results of our global model describe the stellar activity component in a plausible way, and this allowed us to derive a precise and accurate mass estimate for K2-3 b. We also derive a mass for K2-3 c with a significance of less than 3σ. However, using simulations, we demonstrate that our estimate is accurate. Conversely, we do not detect, in our data, the Doppler signal induced by the temperate planet K2-3 d.

Figure 15 shows a planetary mass-radius diagram that includes planets for which the mass and radius were both measured with a relative error better than 30%. Theoretical mass-radius curves for various chemical compositions (Zeng & Sasselov 2013; Zeng et al. 2016) are shown with solid lines. The precision of the radii of the K2-3 planets is mainly limited by that of the stellar radius (all the relative uncertainties are ∼10%; see Table 1). One firm outcome of our analysis is that, for K2-3 b, an Earth-like composition (∼33% of iron and ∼67% of silicates) is rejected with high confidence; we note that in Fig. 15 the masses are represented on a logarithmic scale. Concerning K2-3 c, our mass determination excludes an Earth-like composition with a confidence level of $\sim 4\sigma$ (assuming $R_p = 1.77\ R_\oplus$). The non-detection of K2-3 d was explored in detail through simulations showing that the real Doppler semi-amplitude K_d is likely less than 1 $m\,s^{-1}$ and its corresponding mass is $M_d = 2.7^{+1.2}_{-0.8}\ M_\oplus$ (Sect. 5). Looking at its position on the mass-radius diagram as derived from our simulations, the interior composition of K2-3 d would differ from that of the Earth with a confidence level greater than 2σ in mass and $\sim 2\sigma$ in radius. We note that planets K2-3 c and K2-3 d occupy a region of the mass-radius diagram in which planet occurrence is rare, when only planets with mass and radius measured with a precision better than 30% are considered.

The corresponding bulk densities of all planets ($\rho_p \sim 3$ g cm^{-3}) show that they may have a very similar composition. If further measurements were to confirm our density estimates, excluding rocky compositions for K2-3 c and K2-3 d with higher significance, there are two scenarios that may explain the bulk properties of the K2-3 planets: water-poor planets with H/He envelopes or water worlds.

Several recent studies have investigated the water-poor hypothesis (Lopez 2017; Owen & Wu 2017; Jin & Mordasini 2018; Van Eylen et al. 2017). Fulton et al. (2017) analysed a sample of short-period planetary candidates detected by *Kepler* ($P < 100$ days) and demonstrated that the distribution of planetary radii is bi-modal: the planet candidates have radii that are predominantly either ∼1.3 $R_\oplus$ or ∼2.4 $R_\oplus$, and a gap is observed between 1.5 and 2 $R_\oplus$. The evolutionary model of Owen & Wu (2017) reproduced the observed bi-modal radius distribution in terms of two populations of planets: those consisting of a bare core resulting from photoevaporation, and those with twice the core radius, where the size is doubled by a H/He envelopes. The "gap" detected by Fulton et al. (2017) is actually observed for planets orbiting FGK stars, while the M-dwarf regime was not explored. However, K2-3 is more similar to the FGK sample than to a late-M dwarf, and the results from *Kepler* could still be applicable[15]. Therefore, K2-3 b could have a significant volatile envelope, large enough to measurably change its radius with respect to that of a rocky core. The same may be the case for the other two planets in the K2-3 system, but neither of their radius estimates allow us to unambiguously associate them with one of the groups.

If all planets share the same composition, their densities can be explained by modest primordial hydrogen and helium envelopes atop Earth-like iron and silicate cores. Using the stellar and planet properties derived in this work and assuming a rocky Earth-like core and a solar composition H/He envelope, we find that K2-3 b, c, d are best fit with H/He envelopes comprising 0.7%, 0.3%, and 0.4% of their masses, respectively (Lopez & Fortney 2014). Moreover, using the planetary evolution models of Lopez (2017) we find that none of the planets in this system are vulnerable to losing significant mass through photo-evaporative atmospheric escape.

Even though the water-poor scenario has received a great deal of attention, alternatives should also be considered. Water worlds are planets having massive water envelopes comprising ≥50% of the planet total mass. Recently, bi-modal radius distributions have been derived for the complete *Kepler* sample of Q1–Q17 small exoplanet candidates with radii $R_p < 4\ R_\oplus$ (Zeng et al. 2017a,b). These distributions show that the limits and extent of the radius gap depends on the spectral type of the host star. One proposed explanation for the observed bi-modal distributions is the existence of two populations of planets: rocky worlds, with the lowest radii, and water worlds. The two populations likely share the same underlying rocky component by mass, but differ in the presence of a H_2O-dominated mantle, which is similar to, or slightly more massive than, the rocky component. According to Zeng et al. (2017b), the radius gap for an M0 dwarf such as K2-3 is located at 1.6–1.7 $R_\oplus$. Therefore K2-3 b has an observed mass and radius consistent with that expected for a water world. This could also be the case for K2-3 c and K2-3 d. However, the accuracy of their radii places these planets close to the transition limit that defines the gap, making their water-world membership not highly significant.

We therefore conclude that all three planets in the K2-3 system are likely sub-Neptunes, defined as small, non-rocky planets that have enough volatiles to change their bulk composition measurably. Both the H/He gas envelope and water-world scenarios are possible, particularly for K2-3 b. Based on our data,

[15] An interesting counterexample is represented by planets orbiting the HZ of the late-M-dwarf TRAPPIST-1, which are thought to harbour significant amounts of water (Bourrier et al. 2017), in particular TRAPPIST-1 f (Quarles et al. 2017), showing the diversity of the possible scenarios within the M-dwarf class.

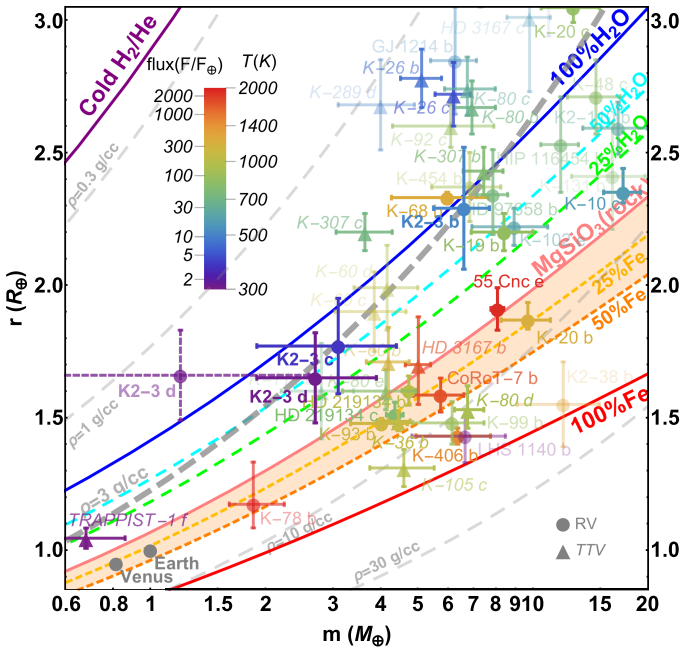

Fig. 15. Mass-radius diagram for exoplanets for which the mass and radius have been both measured with a relative error better than 30%. The location of the K2-3 planets is emphasized. For K2-3 d we also plot the mass derived from the GP analysis (shaded point in violet), and the value corrected using the result of the simulations described in Sect. 5.1. The curve for bulk density ρ = 3 g cm^{-3} is shown in grey passing through the three positions occupied by the K2-3 planets. The planetary data are taken from the NASA exoplanet archive and updated to August 30, 2017.

however, we cannot rule out that K2-3 c and K2-3 d have bare cores of purely rocky, Earth-like composition.

Within the H/He envelope scenario, planets likely formed within the first ∼10 Myr before the dispersion of the gaseous proto-planetary disk. These water-poor planets could have formed in situ, and their similar masses would suggest similar formation histories (Lee & Chiang 2015, 2016). On the other hand, following Ginzburg et al. (2016) one may expect that the planets, during the cooling phase that follows their formation beyond the snow line (e.g. Selsis et al. 2007), were characterized by an intrinsic luminosity that could blow off, over a billion year timescale, any H/He envelope less than about ∼5% by mass. Since a H_2O-layer has a much higher heat capacity than a H/He envelope, this evolutionary pathway could result in water worlds.

If K2-3 d is surrounded by a gaseous envelope, with the properties estimated here, this would likely result in surface pressure and temperatures that are too high to support a habitable planet scenario. A better characterization of K2-3 c and K2-3 d is left to the next generation of high-precision, high-stability spectrographs and to new photometric transit observations. We have shown that an intensive observing sampling over one season with two of the best spectrographs now available would still not have detected a signal with K = 1 m s^{-1} and a period P = 44.5 days. Assuming that our GP result is a good representation of the stellar activity contribution, this means that the true mass of K2-3 d is expected to remain unmeasurable even with a dataset of more than 500 RVs, which is currently not possible for a single target and without a collaboration among various teams. Thus, detecting the real signal induced by K2-3 d is currently very challenging. K2-3 is, however, an ideal target for characterization studies with the VLT/ESPRESSO spectrograph (Pepe et al. 2014), or with near-infrared (NIR) spectrographs such as CARMENES (Quirrenbach et al. 2016), SPIRou (Artigau et al. 2014), and HPF (Mahadevan et al. 2014), provided that they reach their design RV precision and assuming, as expected, that RVs extracted from NIR spectra are less affected by stellar activity.

Acknowledgements. MD acknowledges funding from INAF through the Progetti Premiali funding scheme of the Italian Ministry of Education, University, and Research. We used high performance computing resources made available by INAF through the pilot programme CHIPP (through the proposal Precise planetary mass determination in radial velocity data collected with the HARPS and HARPS-N spectrographs: facing the challenges posed by the time sampling and the presence of stellar noise). We especially thank F. Vitello (INAF-OACt) for his assistance within the CHIPP programme. This research has received funding from the European Union Seventh Framework Programme (FP7/2007-2013) under grant Agreement No. 313014 (ETAEARTH). Parts of this work have been supported by NASA under grants No. NNX15AC90G and NNX17AB59G issued through the Exoplanets Research Program. AVa acknowledges support from the California Institute of Technology (Caltech)/Jet Propulsion Laboratory (JPL) funded by NASA through the Sagan Fellowship Program executed by the NASA Exoplanet Science Institute. PF acknowledges support by Fundação para a Ciência e a Tecnologia (FCT) through Investigador FCT contract of reference IF/01037/2013/CP1191/CT0001, and POPH/FSE (EC) by FEDER funding through the programme "Programa Operacional de Factores de Competitividade - COMPETE". NCS acknowledges support by Fundação para a Ciência e a Tecnologia (FCT, Portugal) through the research grant through national funds and by FEDER through COMPETE2020 by grants UID/FIS/04434/2013 & POCI-01-0145-FEDER-007672 and PTDC/FIS-AST/1526/2014 & POCI-01-0145-FEDER-016886, as well as through Investigador FCT contract nr. IF/00169/2012/CP0150/CT0002.

References

Affer, L., Micela, G., Damasso, M., et al. 2016, A&A, 593, A117
Almenara, J. M., Astudillo-Defru, N., Bonfils, X., et al. 2015, A&A, 581, L7
Anglada-Escudé, G., & Butler, R. P. 2012, ApJS, 200, 15
Anglada-Escudé, G., Tuomi, M., Gerlach, E., et al. 2013, A&A, 556, A126
Anglada-Escudé, G., Amado, P. J., Barnes, J., et al. 2016, Nature, 536, 437
Artigau, É., Kouach, D., Donati, J.-F., et al. 2014, in Ground-based and Airborne Instrumentation for Astronomy V, Proc. SPIE, 9147, 914715
Astudillo-Defru, N., Bonfils, X., Delfosse, X., et al. 2015, A&A, 575, A119
Astudillo-Defru, N., Forveille, T., Bonfils, X., et al. 2017, A&A, 602, A88
Beichman, C., Benneke, B., Knutson, H., et al. 2014, PASP, 126, 1134
Beichman, C., Livingston, J., Werner, M., et al. 2016, ApJ, 822, 39
Benatti, S., Claudi, R., Desidera, S., et al. 2016, in Frontier Research in Astrophysics II, held 23-28 May, 2016, Online at https://pos.sissa.it/cgi-bin/reader/conf.cgi?confid=269, 69
Bonfils, X., Delfosse, X., Udry, S., et al. 2013, A&A, 549, A109
Bonfils, X., Almenara, J. M., Jocou, L., et al. 2015, in Techniques and Instrumentation for Detection of Exoplanets VII, Proc. SPIE, 9605, 96051L
Bonfils, X., Astudillo-Defru, N., Díaz, R., et al. 2018, A&A, 613, A25
Bourrier, V., de Wit, J., Bolmont, E., et al. 2017, AJ, 154, 121
Cloutier, R., Astudillo-Defru, N., Doyon, R., et al. 2017, A&A, 608, A35
Cosentino, R., Lovis, C., Pepe, F., et al. 2014, Ground-based and Airborne Instrumentation for Astronomy V, Proc. SPIE, 9147, 8C
Crossfield, I. J. M., Petigura, E., Schlieder, J. E., et al. 2015, ApJ, 804, 10
Dai, F., Winn, J. N., Albrecht, S., et al. 2016, ApJ, 823, 115
Damasso, M., & Del Sordo F. 2017, A&A, 599, A126
Delfosse, X., Bonfils, X., Forveille, T., et al. 2013a, A&A, 553, A8
Delfosse, X., Donati, J.-F., Kouach, D., et al. 2013b, in SF2A-2013: Proc. of the Annual meeting of the French Society of Astronomy and Astrophysics, eds. L. Cambresy, F. Martins, E. Nuss, & A. Palacios, 497
Dittmann, J. A., Irwin, J. M., Charbonneau, D., et al. 2017, Nature, 544, 333
Dressing, C. D., & Charbonneau, D. 2013, ApJ, 767, 95
Dressing, C. D., & Charbonneau, D. 2015, ApJ, 807, 45
Dressing, C. D., Newton, E. R., Schlieder, J. E., et al. 2017a, ApJ, 836, 167
Dressing, C. D., Vanderburg, A., Schlieder, J. E., et al. 2017b, AJ, 154, 207
Dumusque, X., Borsa, F., Damasso, M., et al. 2017, A&A, 598, A133
Eastman, J., Gaudi, B. S., & Agol, E. 2013, PASP, 125, 83
Feroz, F., & Hobson, M. P. 2014, MNRAS, 437, 3540
Fortier, A., Beck, T., Benz, W., et al. 2014, Space Telescopes and Instrumentation 2014: Optical, Infrared, and Millimeter Wave, Proc. SPIE, 9143, 91432J
Fukui, A., Livingston, J., Narita, N., et al. 2016, AJ, 152, 171
Fulton, B. J., Petigura, E. A., Howard, A. W., et al. 2017, AJ, 154, 109
Giles, H. A. C., Collier Cameron, A., & Haywood, R. D. 2017, MNRAS, 472, 1618
Gillon, M., Triaud, A. H. M. J., Demory, B.-O., et al. 2017, Nature, 542, 456

Ginzburg, S., Schlichting, H. E., & Sari, R. 2016, ApJ, 825, 29
Gomes da Silva, J., Santos, N. C., Bonfils, X., et al. 2011, A&A, 534, A30
Haywood, R. D., Collier Cameron, A., Queloz, D., et al. 2014, MNRAS, 443, 2517
Howell, S. B., Sobeck, C., Haas, M., et al. 2014, PASP, 126, 398
Irwin, J. M., Berta-Thompson, Z. K., Charbonneau, D., et al. 2015, in Cambridge Workshop on Cool Stars, Stellar Systems, and the Sun, eds. G. T. van Belle & H. C. Harris, 18, 767
Jin, S., & Mordasini, C. 2018, ApJ, 853, 163
Kopparapu, R. K., Ramirez, R., Kasting, J. F., et al. 2013, ApJ, 765, 131
Kopparapu, R. K., Ramirez, R. M., SchottelKotte, J., et al. 2014, ApJ, 787, L29
Lee, E. J., & Chiang, E. 2015, ApJ, 811, 41
Lee, E. J., & Chiang, E. 2016, ApJ, 817, 90
Lo Curto, G., Pepe, F., Avila, G., et al. 2015, The Messenger, 162, 9
Lopez, E. D. 2017, MNRAS, 472, 245
Lopez, E. D., & Fortney, J. J. 2014, ApJ, 792, 1
López-Morales, M., Haywood, R. D., Coughlin, J. L., et al. 2016, AJ, 152, 204
Lovis, C., & Pepe, F. 2007, A&A, 468, 1115
Mahadevan, S., Ramsey, L. W., Terrien, R., et al. 2014, in Ground-based and Airborne Instrumentation for Astronomy V, Proc. SPIE, 9147, 91471G
Malavolta, L., Borsato, L., Granata, V., et al. 2017, AJ, 153, 224
Maldonado, J., Affer, L., Micela, G., et al. 2015, A&A, 577, A132
Owen, J. E., & Wu, Y. 2017, ApJ, 847, 29
Pepe, F., Molaro, P., Cristiani, S., et al. 2014, Astron. Nachr., 335, 8
Perger, M., García-Piquer, A., Ribas, I., et al. 2017, A&A, 598, A26
Quarles, B., Quintana, E. V., Lopez, E., Schlieder, J. E., & Barclay, T. 2017, ApJ, 842, L5
Quirrenbach, A., Amado, P. J., Caballero, J. A., et al. 2016, Ground-based and Airborne Instrumentation for Astronomy VI, Proc. SPIE, 9908, 990812
Rauer, H., Catala, C., Aerts, C., et al. 2014, Exp. Astron., 38, 249
Ricker, G. R., Winn, J. N., Vanderspek, R., et al. 2014, Space Telescopes and Instrumentation 2014: Optical, Infrared, and Millimeter Wave, Proc. SPIE, 9143, 20
Robertson, P., Endl, M., Cochran, W. D., & Dodson-Robinson, S. E. 2013, ApJ, 764, 3
Rogers, L. A. 2015, ApJ, 801, 41
Savanov, I. S. 2012, Astron. Rep., 56, 716
Selsis, F., Chazelas, B., Bordé, P., et al. 2007, Icarus, 191, 453
Shields, A. L., Ballard, S., & Johnson, J. A. 2016, Phys. Rep., 663, 1
Sinukoff, E., Howard, A. W., Petigura, E. A., et al. 2016, ApJ, 827, 78
Sozzetti, A., Bernagozzi, A., Bertolini, E., et al. 2013, in EPJ Web Conf., 47, 03006
Tuomi, M., Jones, H. R. A., Barnes, J. R., Anglada-Escudé, G., & Jenkins, J. S. 2014, MNRAS, 441, 1545
Van Eylen, V., Agentoft, C., Lundkvist, M. S., et al. 2017, MNRAS, submitted [arXiv: 1710.05398]
Vanderburg, A., & Johnson, J. A. 2014, PASP, 126, 948
Vanderburg, A., Latham, D. W., Buchhave, L. A., et al. 2016a, ApJS, 222, 14
Vanderburg, A., Plavchan, P., Johnson, J. A., et al. 2016b, MNRAS, 459, 3565
Zechmeister, M., & Kürster, M. 2009, A&A, 496, 577
Zeng, L., & Sasselov, D. 2013, PASP, 125, 227
Zeng, L., Sasselov, D. D., & Jacobsen, S. B. 2016, ApJ, 819, 127
Zeng, L., Jacobsen, S. B., Hyung, E., et al. 2017a, in Lunar and Planetary Inst. Technical Report, Lunar and Planetary Science Conference, 48, 1576
Zeng, L., Jacobsen, S. B., & Sasselov, D. D. 2017b, Research Notes of the AAS, 1, 32

[1] INAF – Osservatorio Astrofisico di Torino, Via Osservatorio 20, 10025 Pino Torinese, Italy
e-mail: damasso@oato.inaf.it

[2] Observatoire de Genève, Université de Genève, 51 ch. des Maillettes, 1290 Sauverny, Switzerland
[3] Université Grenoble Alpes, CNRS, IPAG, 38000 Grenoble, France
[4] Dipartimento di Fisica e Astronomia "Galileo Galilei", Università di Padova, Vicolo dell'Osservatorio 3, 35122 Padova, Italy
[5] INAF – Osservatorio Astronomico di Padova, Vicolo dell'Osservatorio 5, 35122 Padova, Italy
[6] NASA Goddard Space Flight Center, 8800 Greenbelt Rd, Greenbelt, MD 20771, USA
[7] Department of Earth and Planetary Sciences, Harvard University, Cambridge, MA 02138, USA
[8] Harvard-Smithsonian Center for Astrophysics, 60 Garden Street, Cambridge, MA 02138, USA
[9] Centre for Exoplanet Science, SUPA, School of Physics and Astronomy, University of St Andrews, St Andrews KY16 9SS, UK
[10] Department of Astronomy, The University of Texas at Austin, 2515 Speedway, Stop C1400, Austin, TX 78712, USA
[11] INAF – Osservatorio Astronomico di Palermo, Piazza del Parlamento 1, 90134 Palermo, Italy
[12] INAF – Osservatorio Astrofisico di Catania, Via S. Sofia 78, 95123 Catania, Italy
[13] INAF – Osservatorio Astronomico di Trieste, Via Tiepolo 11, 34143 Trieste, Italy
[14] INAF – Osservatorio Astronomico di Brera, Via E. Bianchi 46, 23807 Merate, Italy
[15] Centre for Star and Planet Formation, Niels Bohr Institute & Natural History Museum, University of Copenhagen, 1350 Copenhagen, Denmark
[16] INAF – Fundación Galileo Galilei, Rambla José Ana Fernandez Pérez 7, 38712 Breña Baja, Spain
[17] INAF – Osservatorio Astronomico di Capodimonte, Salita Moiariello 16, 80131 Napoli, Italy
[18] Department of Astronomy, University of California, Berkeley, CA 94720, USA
[19] European Southern Observatory, Alonso de Cordova 3107, Vitacura, Santiago, Chile
[20] Instituto de Astrofísica e Ciências do Espaço, Universidade do Porto, CAUP, Rua das Estrelas, 4150-762 Porto, Portugal
[21] Dipartimento di Fisica, Università di Roma Tor Vergata, Via della Ricerca Scientifica 1, 00133 Roma, Italy
[22] Max Planck Institute for Astronomy, Königstuhl 17, 69117 Heidelberg, Germany
[23] INAF – Osservatorio di Cagliari, via della Scienza 5, 09047 Selargius, CA, Italy
[24] Instituto de Astrofísica de Canarias (IAC), 38200 La Laguna, Tenerife, Spain
[25] Departamento de Astrofísica, Universidad de La Laguna (ULL), 38206 La Laguna, Tenerife, Spain
[26] SUPA, Institute for Astronomy, University of Edinburgh, Royal Observatory, Blackford Hill, Edinburgh EH93HJ, UK
[27] Departamento de Física e Astronomia, Faculdade de Ciências, Universidade do Porto, Rua do Campo Alegre, 4169-007 Porto, Portugal
[28] Astrophysics Research Centre, School of Mathematics and Physics, Queen's University Belfast, Belfast BT7 1NN, UK